CRYSTAL GROWTH & DESIGN

pubs.acs.org/crystal

Article

Tailoring the Phase in Nanoscale $MoTe_2$ Grown by Barrier-Assisted Chemical Vapor Deposition

Christian Martella, Alessio Quadrelli, Pinaka Pani Tummala, Cristina Lenardi, Roberto Mantovan, Alessio Lamperti,* and Alessandro Molle

Cite This: *Cryst. Growth Des.* 2021, 21, 2970–2976

Read Online

ACCESS | Metrics & More | Article Recommendations | Supporting Information

ABSTRACT: We employed chemical vapor deposition (CVD) from powder precursors aiming at large-area growth of molybdenum ditelluride ($MoTe_2$) thin films, with controlled allotropic 2H and 1T′ phases. This major outcome entails tuning the parametric conditions of the precursor fluxes during the deposition. Using a physical barrier, we induce a concentration gradient of the Te precursor, thus enabling the control of the flux fluid dynamics and the formation of a Te-rich or Te-poor environment. As a consequence, the allotropic phase repartition in the films turns out to be determined by the barrier-induced Te concentration, as clearly evidenced by statistical Raman scattering investigations. The effect of the physical barrier is also reflected in the shape of the crystallite population and in their log-normal areal distribution pointing out to a homogeneous nucleation mode of the $MoTe_2$ crystals. Our approach shows the selective allotropic phase control in the barrier-assisted CVD deposition of $MoTe_2$ by adjusting the kinetics of the chemical reaction rather than with the use of growth surfactants.

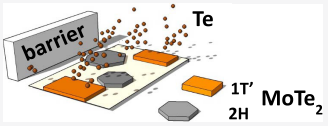

INTRODUCTION

In the realm of two-dimensional (2D) transition-metal dichalcogenides (TMDs), ditellurides, like $MoTe_2$ and WTe_2 have recently attracted increasing interest as they host phase transitions through stable allotropic states with potential application in nanoscience and nanotechnology.[1,2] Transformation from the semiconducting 2H phase to the metallic 1T′ one and vice versa is more readily facilitated in $MoTe_2$, compared to other TMDs due to the relatively smaller energy barrier, therefore making it suitable as robust phase change building blocks in 2D nonvolatile memory devices and memristors.[3,4] Furthermore, the transformation from the semiconducting to the metallic phase, exploiting strategies like strain engineering, envisages novel perspectives from nanoelectronics to catalysis.[5] The 1T′ phase is also the precursor stage to access outstanding topological properties. In the latter respect, the 1T′ phase in ditellurides, orthorhombic in structure, assumes peculiar interest. At the single-layer stage, the 1T′ phase hosts the quantum spin Hall effect, namely, the hallmark of a 2D topological insulating state.[6,7] At the multilayer level, the same phase is again the incubator of a three-dimensional (3D) topological state, known as type-II Weyl semimetal, that takes place in the monoclinic T_d phase as low-temperature distortion of the pristine 1T′ phase.[8,9]

Similar to other TMD growth methods, chemical vapor deposition (CVD) is one of the best candidates aiming at a scalable production of ditellurides enabling the technological application of their peculiar physical and chemical properties. However, tailoring the growth process toward a full control of the phase variability gives a key advantage with exploitation of the full potential of ditellurides, but it is conditioned by the interplay of the thermodynamics and kinetics constraints in the CVD reaction. This fact is quite general for all TMDs, but the process parametric variability becomes particularly decisive in dictating the phase repartition in the ditellurides. This peculiarity is well represented by the case of the tellurization of a predeposited Mo, where one phase can be controllably isolated from another essentially by means of time-dependent process parameters like the carrier gas flow.[10] Such a phenomenology differentiates the details of tellurium reactivity at the Mo or MoO_3 base plane from other chalcogens whose growth results in a polycrystalline layer with nanoscale grains[11,12] and provides tips to reconsider the Te chemistry in other CVD processes. Usually, in sulfides and selenides, the vapor-phase reaction of the two components in the binary compound is the path to achieve nearly perfect 2H microscale crystals.[13−15] Nevertheless, the vapor-phase reaction from bare precursors (MoO_3 and Te) has so far received a relatively scarce consideration in the framework of the chemical vapor deposition of $MoTe_2$ owing to the difficulties in controlling Te chemistry in the process. Tellurium is less reactive than other chalcogens irrespective of the reaction temperature, and the kinetic constraints during the process makes phase tuning and, in particular, single-phase isolation more elusive. To elucidate how phase transformations develop in this scenario, here, we study a barrier-induced concentration gradient of the Te precursor. The target is to define the parametric conditions of

Received: February 2, 2021
Revised: March 23, 2021
Published: March 30, 2021

https://doi.org/10.1021/acs.cgd.1c00130
Cryst. Growth Des. 2021, 21, 2970–2976

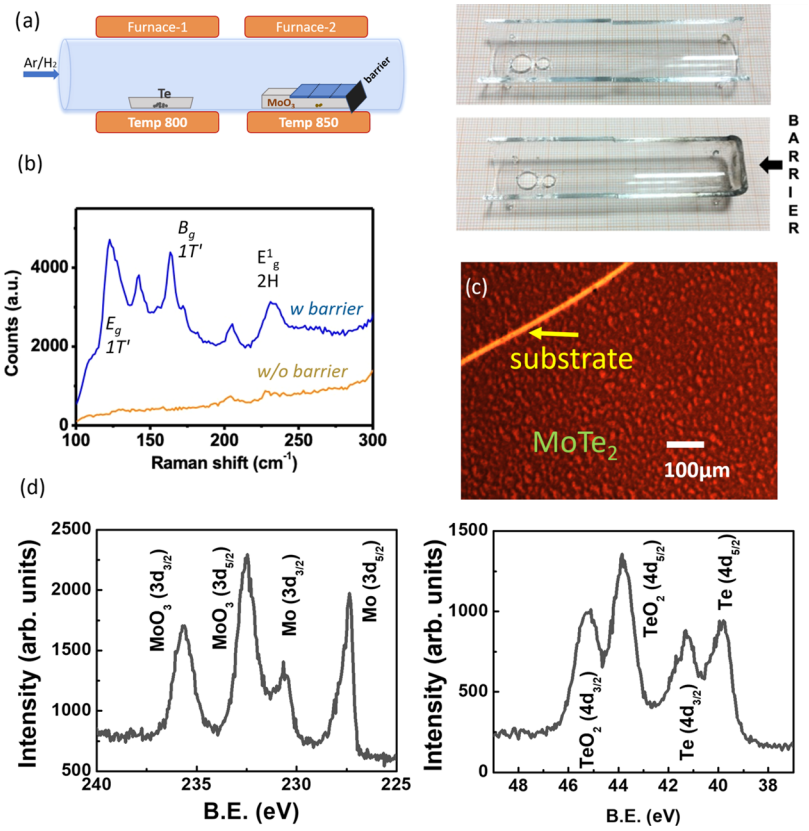

Figure 1. (a) Schematic view of the experimental setup for the barrier-assisted CVD growth of $MoTe_2$ films. (Right) Glass boat containing the MoO_3 powder and the substrate without the glass barrier (top) and with the barrier (bottom). (b) Raman spectra of the $MoTe_2$ film obtained with (blue trace) and without (orange trace) barrier. (c) Large-area optical image of the $MoTe_2$ film obtained by the barrier-assisted CVD approach. A scratch, in the top-left corner of the image, demonstrates the homogeneity of the deposition (d) Mo (3d) and Te (4d) spectral regions from X-ray photoelectron spectroscopy (XPS); the oxide component is coming from a thin layer at the surface due to exposure to the atmosphere (see the Supporting Information).

the 1T′-$MoTe_2$ formation from a vapor-phase reaction approach with no use of growth surfactants.[16] We show that a mechanical barrier at the edge of the quartz boat accommodating the growth substrate is mandatory for the $MoTe_2$ growth to start up. In addition, we elucidate the details of the $MoTe_2$ nucleation to assess the stability of the 1T′ phase against parametric variability of the process.

MATERIALS AND METHODS

Materials Growth. $MoTe_2$ crystals were grown on a SiO_2 (50 nm)/Si substrate in a CVD apparatus (planarTECH LLC). A quartz tube was used as the reaction chamber, and two furnaces were used to set up upstream and downstream heating zones. The quartz tube has a diameter of 2 in. and a total length of 146 cm. In the upstream zone, we loaded 100 mg of tellurium powder (99.998%, Sigma-Aldrich), while ∼24 cm away, in the downstream region, 1 mg of MoO_3 (99.98%, Sigma-Aldrich) was placed in a quartz boat. The quartz boats are approximately shaped in a half-cylinder cut along the long axis (height). The base has a radius (r) of 1 cm, while the height (h) is 7 cm; see Figure S1. The substrate was placed directly on top of the boat, facing the MoO_3 powder. The system was pumped down to a pressure of 3×10^{-4} mbar and purged with 1000 sccm high-purity argon for several minutes. The different thermal ramps adopted in the CVD processes are discussed in the following sections. The maximum temperatures reached in the upstream furnace (tellurium region) and downstream furnace (MoO_3 region) were 800 and 850 °C, respectively (see Figure 1a). The system was naturally cooled down to room temperature, and 1000 sccm Ar flow was used to remove the reactants.

Sample Characterization. Raman spectroscopy measurements were performed in a backscattering configuration employing a Renishaw InVia spectrometer, equipped with the 514 nm (2.41 eV) line of a solid-state diode laser. The laser radiation was focused on the sample by means of a 50× Leica objective (0.75 numerical aperture), maintaining the incident laser power below 1 mW to avoid sample damage. The morphology of the sample was characterized using a Zeiss-SUPRA 40 field-emission scanning electron microscope (SEM) in bright-field mode. Chemical composition was probed using an XPS PHI ESCA 5600 with a monochromatic Al X-ray source and a hemispherical analyzer with pass energy 5.85 eV, energy step 0.025 eV, and energy resolution >0.1 eV.

RESULTS AND DISCUSSION

A thermodynamically favored condition for the emergence of a prevailing 1T′ phase in $MoTe_2$ is known to take place when the substrate temperature is brought over 800 °C, as reported in the case of salt-assisted CVD.[16] After setting a growth temperature of 850 °C in a double-furnace CVD reactor under isobaric condition (pressure, 1 atm/760 torr) and with a 10 sccm Ar/H_2 flux (H_2 4% vol) as a carrier gas (see Figure 1a for a scheme of the apparatus), we note that an essential requirement for $MoTe_2$ to grow was the presence of a mechanical barrier at the downstream edge of the quartz boat hosting the substrate that serves as a physical obstacle for the vapor flux during the CVD process. This is reflected in the comparative Raman spectrum acquired after CVD growth with and without the blocking barrier in Figure 1b. The absence of

https://doi.org/10.1021/acs.cgd.1c00130
Cryst. Growth Des. 2021, 21, 2970−2976

the blocking barrier gives no yield in terms of materials growth (poor Raman intensity in the spectrum), while the characteristic Raman spectrum of $MoTe_2$ is observed when employing the blocking barrier, which plays the role to redirect the two main vapor fluxes (MoO_3 vapor from the boat and Ar-transported Te flux); see Figure 1a. This scenario will be further clarified in the following while examining the effect of the Ar flux and hence, the Te transport on the $MoTe_2$ growth. The Raman spectrum recorded in the case of a barrier-assisted CVD (see Figure 1b, blue curve, and Figure S2 in the Supporting Information) exhibits well-defined peaks at 164, 107, and 123 cm^{-1} that are indicative of an interplay of domains with 1T′ and 2H phases.[17] The more intense peak at 164 cm^{-1} is assigned to the B_g mode of the 1T′ phase.[17] Other features of the 1T′ phase are the Raman peaks at 107, 123, and 257 cm^{-1} corresponding to the A_u, E_{1g}, and A_g modes.[18,19] The fingerprints of the 2H phase of the $MoTe_2$ are the intense and relatively broader peaks at 230 and 180 cm^{-1} that are assigned to the $E_{2g}{}^1$, A_g modes, respectively.[17] As previously proposed,[18] the relative proportion of the 1T′ and 2H phases can be deduced by taking into account the B_g and $E_{2g}{}^1$ peak intensities according to the following relations (equation 1)

$$R_{1T'} = \frac{I_{B_g}}{I_{B_g} + I_{E^1_{2g}}}, \quad R_{2H} = 1 - R_{1T'} \tag{1}$$

where the intensities of the Raman peaks are derived from the fit to the data as reported in Figure S2 in the Supporting Information.

The successful growth of $MoTe_2$ is confirmed from XPS measurements. Figure 1d reports the high-resolution XPS spectra from Mo(3d) and Te(4d) core levels. Considering Mo(3d), the presence of 2 Mo chemical states, each with its spin−orbit splitting, is clear. We observe a Mo chemical state at binding energies of 227.4 eV (5/2) and 230.6 eV (3/2) that we associate with the bonding of Mo with Te to form $MoTe_2$.[17] Further, we observe the emergence of an additional Mo chemical state at binding energies of 232.5 eV (5/2) and 235.6 eV (3/2) that we attribute to oxide MoO_3. Considering the Te(4d) spectral region, we observe a similar situation to that in Mo(3d), with the evidence of 2 Te chemical states, each with its spin−orbit splitting components. In particular, we observe the presence of a Te chemical state at binding energies of 39.8 eV (5/2) and 41.2 eV (3/2) that we attribute to the bonding of Te with Mo to form $MoTe_2$.[17] In addition, we observe second Te chemical states at binding energies of 43.8 eV (5/2) and 45.2 eV (3/2) that we associate with the TeO_2 oxide form. In consideration of the extreme surface sensitivity of the technique, to ascertain the location of the oxidized contributions, we collected Te(3d) spectra before and after 1 min Ar sputtering. As shown in Figure S2c in the Supporting Information, the peaks associated with the TeO_2 chemical state vanish after the sputtering, meaning that the oxidation is limited to the uppermost layers and the synthesized material consists of pure $MoTe_2$. The presence of the oxidation layer is due to the exposure to the ambient before ex situ XPS and suggests the degree of degradation of the as-grown $MoTe_2$ in the presence of oxygen.

The optical microscope image in Figure 1c displays a large-area coverage of the $MoTe_2$ layer grown by barrier-assisted CVD that is consistent with the statistical Raman analysis vs. position. A deeper insight into the film microstructure is gained in Figure 2a by high-resolution SEM imaging of the

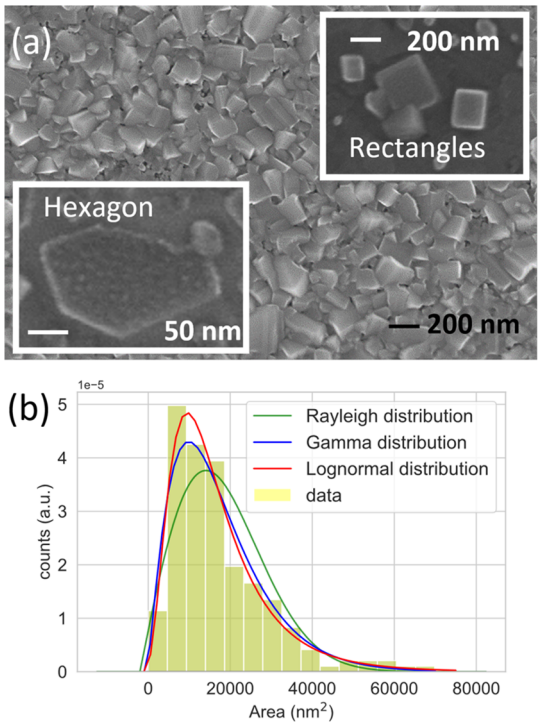

Figure 2. (a) Large-area and high-resolution (insets) SEM images showing the $MoTe_2$ crystallites with characteristic rectangular and hexagonal shapes. (b) Histogram of the crystallite-area distribution fitted to Rayleigh, Γ, and log-normal distributions.

morphological features at the microscopic level. Based on Figure 2a, the layer is continuous on the 100 μm scale and the morphology displays a texture of crystallites with shape variability, i.e., majority rectangular domains vs minority hexagonal and triangular ones (see the insets of Figure 2a). These characteristic geometries can be assigned to 1T′ and 2H crystallites, respectively, as previously reported[14,20] and in agreement with the concomitant presence of 1T′ and 2H features in the Raman spectrum of Figure 1b. The so-observed shape variability reflects the balance between the two $MoTe_2$ phases despite the growth condition is expected to be thermodynamically 1T′ phase-selective. Nonetheless, in the given process scheme, we note that the crystallite population is quite dominated by the rectangular crystallites, namely, by a majority 1T′ phase, the hexagonal-shaped domain being a relatively small amount of the surface structures. The related areal distribution is then reminiscent of the nucleation mode because its statistical behavior can be rationalized by fitting functions that are influenced by different physical constraints at the early stages of the growth. This is reported as a histogram plot in Figure 2b, where the data are interpolated by means of three possible fitting functions, namely, log-normal, Γ, and Rayleigh functions. Best fit to the data is gained with a log-normal function [$\chi^2 = 0.40$] with a mean value of 0.57, with a slight difference from the Γ function [$\chi^2 = 0.75$] and a large margin with respect to the Rayleigh one [$\chi^2 = 8.3$], where χ^2 is the reduced chi square. Generally speaking, log-normal and Γ functions describe independent events (following a Poisson statistics) which are progressive, i.e., temporally separated, and simultaneous, respectively.[21,22] In the areal distribution, we neglected the contribution of overlapping crystals by noting that the largest part of the crystal edges is exposed; see the false-color image in Figure S3a. A further argument supporting

https://doi.org/10.1021/acs.cgd.1c00130
Cryst. Growth Des. 2021, 21, 2970−2976

our conclusion is provided by the analysis of Figure S3b, where crystallites are clearly well separated. The histogram of the areal distribution (Figure S3c) confirms that, also in this case, the log-normal function is the best-fitting option with χ^2 = 1.63. As a result of the analysis, we conclude that the experimentally derived areal distribution points out to a homogeneous nucleation where the growth of a nucleus is a random event that is independent of the others. In other words, $MoTe_2$ nucleation is not driven by a bias, like the coalescence or preferential surface diffusion channeling, nor subjected to coarsening, but it takes place at different times, with nuclei forming while other ones are already formed. This aspect rationalizes the fact that grains with different sizes are observed in the grown layer.

Given the kinetic character of the nucleation and its influence on the later stages of the crystal growth, we are concerned to know how the crystallite structure can be inverted from the observed 1T′ majority toward the 2H phase by changing the growth kinetics. The latter is governed by CVD's dynamic parameters such as the velocity of the Te transport, which in turn can be tuned as a function of the carrier gas flux (ϕ). Indeed, ϕ is reported to play a decisive role in switching from one phase to the other in the tellurization of a Mo film.[10] The relevant phenomenology of vapor-phase reaction as a function of ϕ is elucidated by the Raman spectra in Figure 3. A positional variability of the $MoTe_2$ phase is

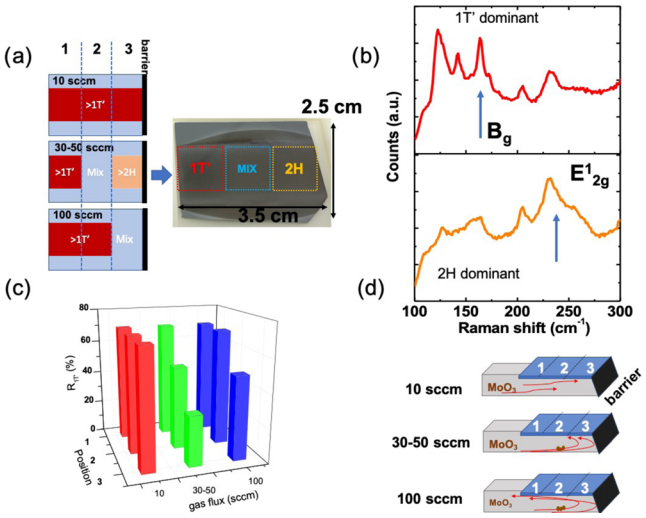

Figure 3. (a) Schematic and optical view of the samples. (b) Raman spectra showing, respectively, the dominant 1T′ (red) and 2H (orange) phases. (c) Histograms of the relative 1T′ proportion in the samples as a function of the carrier gas flux and positions 1, 2, and 3 on the sample surface as shown in (a). Each point in the histogram is the average over 10 spectra taken in a millimeter-scaled area inside the given region where no changes appear in the optical microscope image. (d) Sketches of the barrier-induced Te concentration mechanism as a function of the gas flux.

observed by comparing the Raman spectra from three uniform regions in the sample (see Figure 3a). In detail, regions 1 and 3 point out to edge zones of the samples, i.e., far from and close to the blocking barrier, respectively, whereas region 2 is an intermediary zone in between the other two (see the sketch and the optical images in Figure 3a). Each region extends in the flux direction for ∼1 cm, while the lateral width ∼1.5 cm is dictated by the geometrical dimension of the silica boat in use.

At a low flux (ϕ = 10 sccm), the Raman spectrum is qualified by an intense B_g peak and a minor E_{2g}^1 peak, therefore manifesting a majority 1T′ phase in the $MoTe_2$ structure over the whole sample (regions 1−3, Figure 3b). Increasing ϕ in the range of 30−50 sccm leads to the emergence of a majority 2H phase ($R_{1T'}$ = 30%, R_{2H} = 70%) in the proximity of the glass barrier (region 3), while a mixed phase ($R_{1T'} = R_{2H}$ = 50%) is found at region 2. Throughout region 1, a majority 1T′ phase ($R_{1T'}$ = 70%) is restored (see Figure S1b in the Supporting Information). This 1T′ majority condition is restored over the whole sample area increasing ϕ up to 100 sccm. The overall scenario is summarized in the histogram of Figure 3c, where $R_{1T'}$, deduced from equation 1, is plotted as a function of ϕ for regions 1, 2, and 3. Each point in the histogram is the average over 10 spectra taken in a millimeter-scaled area inside the given region, where no changes appear in the optical microscope image.

The phase diagram in Figure 3c reflects the emergence of a majority 2H phase only at ϕ = 30−50 sccm and in the proximity of the glass barrier (region 3), while the 1T′ phase formation is favored ($R_{1T'}$ = 68%) at flux values ϕ < 10 sccm and ϕ > 30 sccm in all regions detected. Basically, the observed behavior resembles a similar trend to that reported for the tellurization,[10] this fact being due to the kinetic constraints for the formation of one phase when the stationary Te concentration in the reaction ambient is varied. Conversely, the positional variability can be rationalized in terms of the vapor fluid dynamics induced by the blocking barrier with different carrier flux applied. We stress that, in our experimental scheme, the vertical distance between the MoO_3 powder and the substrate has been kept fixed to avoid additional vapor fluid-dynamic modification. We propose a representative picture of the barrier mechanism in Figure 3d. In detail, in the low-flux regime (ϕ = 10 sccm), the carrier gas-assisted tellurium transport from its pristine boat to the reaction site is slow enough to give rise to a tellurium-poor environment. This Te-deficient condition induces the preferential formation of the 1T′ phase throughout the whole sample area (regions 1, 2, and 3; see Figure 3d, top) consistent with the case of tellurization.[10] Increasing the flux in the 30−50 sccm range results in an increased concentration of tellurium precursor in the vapor phase in the proximity of the glass barrier (region 3), thus creating the favorable condition for the 2H phase to form while farther regions (1 and 2) still suffer from a Te-deficient environment, and hence, they grow with a 1T′ phase, mainly (Figure 3d, middle). The high-flux regime (ϕ = 100 sccm) reduces the residing time for the evaporating Te atoms since the Te flux is scattered back from the blocking barrier (Figure 3d, bottom). As a consequence, no tellurium-rich atmosphere is reached in the reaction zones, thus giving rise to the 1T′ phase again. The effectiveness of the convective motions is demonstrated by Te precipitation on substrate placed upstream (see Figure S4 in the Supporting Information), i.e., against the carrier gas flow. As a consequence, the 2H phase occurring at a low ϕ results from a Te-rich concentration and the growth dynamics is hence concentration-limited.

On the other hand, the stationary concentration of tellurium, namely, the amount of Te provided during the process, is another key parameter for the selection of a preferential phase. To determine the role of the Te concentration in the Mo−Te reaction, we vary the Te partial pressure in the flux window, where the 2H phase occurs in the proximity of the glass barrier,

https://doi.org/10.1021/acs.cgd.1c00130
Cryst. Growth Des. 2021, 21, 2970−2976

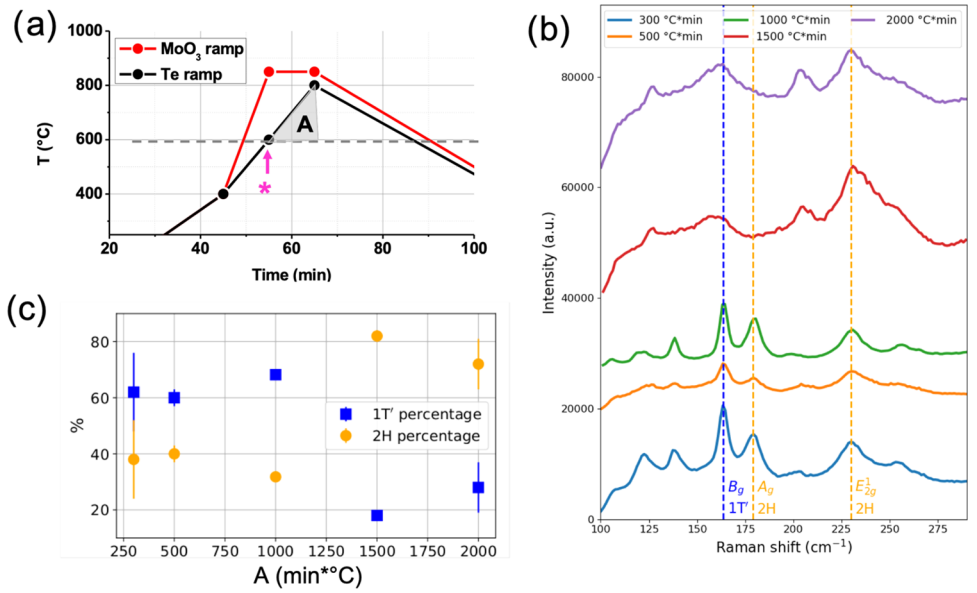

Figure 4. (a) Thermal ramps of the $MoTe_2$ growth. The integral tellurium concentration provided throughout the growth is proportional to the area of the triangle denoted by A. Moving the experimental point "*" toward right in the time scale, the area of the triangle is varied. (b) Raman spectra at different integral Te concentrations. (c) Relative proportion of 1T′ and 2H phase as a function of the integral tellurium concentration provided throughout the growth. The fraction of the 1T′ phase is calculated as the statistical mean of the $R_{1T'}$ coefficients obtained in regions 1, 2, and 3 based on the average of 10 Raman spectra taken in a millimeter-scaled area for each region. The uncertainty of each point has been calculated considering the standard deviation of the data from the mean value.

namely, at ϕ = 30 sccm in region 3. The Te evaporation rate is controlled by means of the temperature ramp rate ΔT at the Te source, while keeping the carrier gas flux at 30 sccm according to the process flow diagram in Figure 4a. In this respect, the Te partial pressure is proportional to the evaporation rate; see Figure S5 in the Supporting Information. The temperature ramp rate ΔT is varied moving toward right in the horizontal (time) scale the experimental point denoted by "*" in Figure 4a. The Te concentration in the process is then derived as the time integral of the evaporation rate, being proportional to the triangular area A as indicated in Figure 4a. When A is varied from 250 to 2000 min*°C (Figure 4c), a dramatic change can be observed in the characteristic features of the Raman spectrum. However, at a low A, the 1T′-related features definitely prevail, qualified by the emergence of dominant B_g peak in the Raman spectrum, and the gradual increase of the Te concentration leads to a dominant 2H phase (Figure 4b). In fact, qualitatively, both 1T′ and 2H phases coexist throughout the whole A-range considered, with their relative abundance being adjustable by tuning the Te concentration. To provide a quantitative description of the phase engineering process, we report in Figure 4c the phase proportion deduced from the Raman spectra through eq 1. The fraction of the 1T′ phase is calculated as the statistical mean of the $R_{1T'}$ coefficients obtained in regions 1, 2, and 3 based on the average of 10 Raman spectra taken in a millimeter-scaled area for each region. The uncertainty of each point has been calculated considering the standard deviation of the data from the mean value. It can be immediately noted that the onset for a majority 2H phase formation (with R_{2H} = 80%) takes place at a threshold $A \geq 1500$ min*°C. For a given flux of 30 sccm, this condition stably holds on with rate amounting up to 2000 min*°C. Conversely, an almost constant $R_{1T'}$ = 60% is observed in the subthreshold Te concentration range. Our results evidence that the phase transitions under isothermal condition are crucially driven by the Te concentration at the reaction point, with 2H (1T′) phase resulting from a Te-rich (Te-poor) environment with the evaporating MoO_3 at the substrate, respectively. This conclusion is consistent with the concentration-limited growth condition observed in the flux dependency (see Figure 3).

CONCLUSIONS

The chemical vapor co-deposition from MoO_3 and Te vapor effectively results in a $MoTe_2$ growth only when the vapor fluxes are physically blocked by a downstream positioned glass barrier. This mechanical stopper acts as a fluid dynamics controller of the vapor reaction, thereby generating Te-poor and Te-rich conditions during the $MoTe_2$ nucleation. This is key-trim to dictate the phase selection in the $MoTe_2$ nucleation in between a semiconducting 2H phase and a topologically interesting 1T′ one. In particular, the reactive co-deposition of $MoTe_2$ in a thermal regime, where the 1T′ phase is thermodynamically stable, discloses a kinetic scenario, where the proportion of the 1T′ and 2H phase is a tellurium concentration-limited mechanism. This scenario is reflected in a log-normal distribution of the crystallite grain size in the $MoTe_2$ film, which we rationalize as a homogeneous, random, and progressive nucleation of $MoTe_2$ clusters with a rectangular shape (1T′ phase) or hexagonal shape (2H phase). We show that these mechanisms can be readily mastered by introducing a physical barrier in the reactor, thus inducing a concentration gradient of the tellurium precursor. Moreover, by tailoring the relevant process parameters, such as the temperature ramp and the carrier gas flux, the full control of the phase proportion in the grown $MoTe_2$ is achieved. In particular, we conclude that the environmental Te is a necessary condition to tune a Te-rich or Te-poor environment, thus leading to a dominant 2H or 1T′ phase, respectively. However, not only the Te concentration matters, but also the Te transport velocity affects the Te reactivity. Overall, we

https://doi.org/10.1021/acs.cgd.1c00130
Cryst. Growth Des. 2021, 21, 2970−2976

succeeded in determining the kinetical conditions to have phase selectivity in nanoscaled $MoTe_2$ through a vapor-phase reaction approach, thus paving the way to the exploitation of phase-selected $MoTe_2$ for specific applications in nanoelectronics exploiting strain engineering[5] and topological properties.[23,24]

■ ASSOCIATED CONTENT

Supporting Information

The Supporting Information is available free of charge at https://pubs.acs.org/doi/10.1021/acs.cgd.1c00130.

Additional Raman spectra of the grown material, XPS spectra after sputtering, SEM images and statistical analysis of the areal distribution of crystallites, schematic view of the silica boats used in the CVD growth, optical picture and SEM image of the tellurium redeposition at a high carrier gas flux, and plot of tellurium vapor pressure vs time for different temperature rates in the CVD growth (PDF)

■ AUTHOR INFORMATION

Corresponding Author

Alessio Lamperti − *CNR-IMM, Unit of Agrate Brianza, 20864 Agrate Brianza, MB, Italy;* orcid.org/0000-0003-2061-2963; Email: alessio.lamperti@mdm.imm.cnr.it

Authors

Christian Martella − *CNR-IMM, Unit of Agrate Brianza, 20864 Agrate Brianza, MB, Italy;* orcid.org/0000-0003-1811-165X

Alessio Quadrelli − *C.I.Ma.I.Na., Dipartimento di Fisica, Università degli Studi di Milano, 20133 Milano, Italy*

Pinaka Pani Tummala − *CNR-IMM, Unit of Agrate Brianza, 20864 Agrate Brianza, MB, Italy*

Cristina Lenardi − *C.I.Ma.I.Na., Dipartimento di Fisica, Università degli Studi di Milano, 20133 Milano, Italy;* orcid.org/0000-0002-5522-6803

Roberto Mantovan − *CNR-IMM, Unit of Agrate Brianza, 20864 Agrate Brianza, MB, Italy;* orcid.org/0000-0002-9353-4137

Alessandro Molle − *CNR-IMM, Unit of Agrate Brianza, 20864 Agrate Brianza, MB, Italy;* orcid.org/0000-0002-3860-4120

Complete contact information is available at: https://pubs.acs.org/10.1021/acs.cgd.1c00130

Author Contributions

All authors have given approval to the final version of the manuscript.

Funding

R.M. received financial support from the Horizon 2020 project SKYTOP "Skyrmion-Topological Insulator and Weyl Semimetal Technology" (FETPROACT-2018-01, no 824123). A.L. received financial support from Ministero dell'Istruzione, dell'Università e della Ricerca (MIUR) under the project PRIN 2017 aSTAR, grant 2017RKWTMY.

Notes

The authors declare no competing financial interest.

■ ACKNOWLEDGMENTS

The authors acknowledge Mario Alia (CNR-IMM) for technical support. C.M. acknowledges Prof. Liu Zheng and Dr. Jiadong Zhou (Nanyang Technological University) for fruitful discussion.

■ REFERENCES

(1) Zhou, L.; Zubair, A.; Wang, Z.; Zhang, X.; Ouyang, F.; Xu, K.; Fang, W.; Ueno, K.; Li, J.; Palacios, T.; Kong, J.; Dresselhaus, M. S. Synthesis of High-Quality Large-Area Homogenous 1T′ MoTe2 from Chemical Vapor Deposition. *Adv. Mater.* **2016**, *28*, 9526−9531.

(2) Zhou, J.; Liu, F.; Lin, J.; Huang, X.; Xia, J.; Zhang, B.; Zeng, Q.; Wang, H.; Zhu, C.; Niu, L.; Wang, X.; Fu, W.; Yu, P.; Chang, T.-R.; Hsu, C.-H.; Wu, D.; Jeng, H.-T.; Huang, Y.; Lin, H.; Shen, Z.; Yang, C.; Lu, L.; Suenaga, K.; Zhou, W.; Pantelides, S. T.; Liu, G.; Liu, Z. Large-Area and High-Quality 2D Transition Metal Telluride. *Adv. Mater.* **2017**, *29*, No. 1603471.

(3) Zhang, F.; Zhang, H.; Krylyuk, S.; Milligan, C. A.; Zhu, Y.; Zemlyanov, D. Y.; Bendersky, L. A.; Burton, B. P.; Davydov, A. V.; Appenzeller, J. Electric-Field Induced Structural Transition in Vertical MoTe2- and Mo1−XWxTe2-Based Resistive Memories. *Nat. Mater.* **2019**, *18*, 55−61.

(4) Sun, L.; Ding, M.; Li, J.; Yang, L.; Lou, X.; Xie, Z.; Zhang, W.; Chang, H. Phase-Controlled Large-Area Growth of MoTe2 and MoTe2-XOx/MoTe2 Heterostructures for Tunable Memristive Behavior. *Appl. Surf. Sci.* **2019**, *496*, No. 143687.

(5) Martella, C.; Mennucci, C.; Lamperti, A.; Cappelluti, E.; de Mongeot, F. B.; Molle, A. Designer Shape Anisotropy on Transition-Metal-Dichalcogenide Nanosheets. *Adv. Mater.* **2018**, *30*, No. 1705615.

(6) Tang, S.; Zhang, C.; Wong, D.; Pedramrazi, Z.; Tsai, H.-Z.; Jia, C.; Moritz, B.; Claassen, M.; Ryu, H.; Kahn, S.; Jiang, J.; Yan, H.; Hashimoto, M.; Lu, D.; Moore, R. G.; Hwang, C.-C.; Hwang, C.; Hussain, Z.; Chen, Y.; Ugeda, M. M.; Liu, Z.; Xie, X.; Devereaux, T. P.; Crommie, M. F.; Mo, S.-K.; Shen, Z.-X. Quantum Spin Hall State in Monolayer 1T′-WTe2. *Nat. Phys.* **2017**, *13*, 683−687.

(7) Qian, X.; Liu, J.; Fu, L.; Li, J. Quantum Spin Hall Effect in Two-Dimensional Transition Metal Dichalcogenides. *Science* **2014**, *346*, 1344−1347.

(8) Soluyanov, A. A.; Gresch, D.; Wang, Z.; Wu, Q.; Troyer, M.; Dai, X.; Bernevig, B. A. Type-II Weyl Semimetals. *Nature* **2015**, *527*, 495−498.

(9) Sun, Y.; Wu, S.-C.; Ali, M. N.; Felser, C.; Yan, B. Prediction of Weyl Semimetal in Orthorhombic MoTe2. *Phys. Rev. B* **2015**, *92*, No. 161107.

(10) Yang, L.; Zhang, W.; Li, J.; Cheng, S.; Xie, Z.; Chang, H. Tellurization Velocity-Dependent Metallic-Semiconducting-Metallic Phase Evolution in Chemical Vapor Deposition Growth of Large-Area, Few-Layer MoTe2. *ACS Nano* **2017**, *11*, 1964−1972.

(11) Vangelista, S.; Cinquanta, E.; Martella, C.; Alia, M.; Longo, M.; Lamperti, A.; Mantovan, R.; Basset, F. B.; Pezzoli, F.; Molle, A. Towards a Uniform and Large-Scale Deposition of MoS 2 Nanosheets via Sulfurization of Ultra-Thin Mo-Based Solid Films. *Nanotechnology* **2016**, *27*, No. 175703.

(12) Martella, C.; Melloni, P.; Cinquanta, E.; Cianci, E.; Alia, M.; Longo, M.; Lamperti, A.; Vangelista, S.; Fanciulli, M.; Molle, A. Engineering the Growth of MoS2 via Atomic Layer Deposition of Molybdenum Oxide Film Precursor. *Adv. Electron. Mater.* **2016**, *2*, No. 1600330.

(13) Wang, X.; Gong, Y.; Shi, G.; Chow, W. L.; Keyshar, K.; Ye, G.; Vajtai, R.; Lou, J.; Liu, Z.; Ringe, E.; Tay, B. K.; Ajayan, P. M. Chemical Vapor Deposition Growth of Crystalline Monolayer MoSe 2. *ACS Nano* **2014**, *8*, 5125−5131.

(14) Wang, S.; Rong, Y.; Fan, Y.; Pacios, M.; Bhaskaran, H.; He, K.; Warner, J. H. Shape Evolution of Monolayer MoS 2 Crystals Grown by Chemical Vapor Deposition. *Chem. Mater.* **2014**, *26*, 6371−6379.

(15) Lee, Y.-H.; Zhang, X.-Q.; Zhang, W.; Chang, M.-T.; Lin, C.-T.; Chang, K.-D.; Yu, Y.-C.; Wang, J. T.-W.; Chang, C.-S.; Li, L.-J.; Lin, T.-W. Synthesis of Large-Area MoS2 Atomic Layers with Chemical Vapor Deposition. *Adv. Mater.* **2012**, *24*, 2320−2325.

(16) Keum, D. H.; Cho, S.; Kim, J. H.; Choe, D.-H.; Sung, H.-J.; Kan, M.; Kang, H.; Hwang, J.-Y.; Kim, S. W.; Yang, H.; Chang, K. J.;

Lee, Y. H. Bandgap Opening in Few-Layered Monoclinic MoTe2. *Nat. Phys.* **2015**, *11*, 482−486.
(17) Sun, Y.; Zhuang, P.; Jiang, W.; Xu, H.; Zhang, S.; Xuan, N.; Ba, K.; Liu, H.; Wang, J.; Bao, W.; Shen, J.; Sun, Z. Phase, Conductivity, and Surface Coordination Environment in Two-Dimensional Electrochemistry. *ACS Appl. Mater. Interfaces* **2019**, *11*, 25108−25114.
(18) Xu, X.; Li, X.; Liu, K.; Li, J.; Feng, Q.; Zhou, L.; Cui, F.; Liang, X.; Lei, Z.; Liu, Z.; Xu, H. Thermodynamics and Kinetics Synergetic Phase-Engineering of Chemical Vapor Deposition Grown Single Crystal MoTe2 Nanosheets. *Cryst. Growth Des.* **2018**, *18*, 2844−2850.
(19) Empante, T. A.; Zhou, Y.; Klee, V.; Nguyen, A. E.; Lu, I.-H.; Valentin, M. D.; Naghibi Alvillar, S. A.; Preciado, E.; Berges, A. J.; Merida, C. S.; Gomez, M.; Bobek, S.; Isarraraz, M.; Reed, E. J.; Bartels, L. Chemical Vapor Deposition Growth of Few-Layer MoTe 2 in the 2H, 1T′, and 1T Phases: Tunable Properties of MoTe 2 Films. *ACS Nano* **2017**, *11*, 900−905.
(20) Sung, J. H.; Heo, H.; Si, S.; Kim, Y. H.; Noh, H. R.; Song, K.; Kim, J.; Lee, C.-S.; Seo, S.-Y.; Kim, D.-H.; Kim, H. K.; Yeom, H. W.; Kim, T.-H.; Choi, S.-Y.; Kim, J. S.; Jo, M.-H. Coplanar Semiconductor−Metal Circuitry Defined on Few-Layer MoTe2 via Polymorphic Heteroepitaxy. *Nat. Nanotechnol.* **2017**, *12*, 1064−1070.
(21) Bergmann, R. B.; Bill, A. On the Origin of Logarithmic-Normal Distributions: An Analytical Derivation, and Its Application to Nucleation and Growth Processes. *J. Cryst. Growth* **2008**, *310*, 3135−3138.
(22) Fátima Vaz, M.; Fortes, M. A. Grain Size Distribution: The Lognormal and the Gamma Distribution Functions. *Scr. Metall.* **1988**, *22*, 35−40.
(23) Safeer, C. K.; Ontoso, N.; Ingla-Aynés, J.; Herling, F.; Pham, V. T.; Kurzmann, A.; Ensslin, K.; Chuvilin, A.; Robredo, I.; Vergniory, M. G.; de Juan, F.; Hueso, L. E.; Calvo, M. R.; Casanova, F. Large Multidirectional Spin-to-Charge Conversion in Low-Symmetry Semimetal MoTe2 at Room Temperature. *Nano Lett.* **2019**, *19*, 8758−8766.
(24) Liang, S.; Shi, S.; Hsu, C.; Cai, K.; Wang, Y.; He, P.; Wu, Y.; Pereira, V. M.; Yang, H. Spin-Orbit Torque Magnetization Switching in MoTe2/Permalloy Heterostructures. *Adv. Mater.* **2020**, *32*, No. 2002799.

https://doi.org/10.1021/acs.cgd.1c00130
Cryst. Growth Des. 2021, 21, 2970−2976